Solar Phys (2014) 289:193–209
DOI 10.1007/s11207-013-0334-4

Statistical Moments of Active-Region Images During Solar Flares

S. Šimberová · M. Karlický · T. Suk

Received: 27 August 2012 / Accepted: 20 May 2013 / Published online: 20 July 2013
© Springer Science+Business Media Dordrecht 2013

Abstract We present new temporal-evolution diagnostics of solar flares. The high-order statistical moments (skewness and kurtosis) of the Hα images of active regions during solar flares were computed from their initial phases up to their maxima. The same method was used for quiet active regions for tests and comparison. We found that temporal profiles of the Hα statistical moments during flares roughly correspond to those observed in soft X-rays by the GOES satellite. Maxima of the cross-correlation coefficients between the skewness and the GOES X-rays were found to be 0.82 – 0.98, and the GOES X-rays are delayed 0 – 144 seconds against the skewness. We recognized that these moments are very sensitive to pre-flare activities. Therefore we used them to determine the flare starting-time and to study the pre-flare quasi-periodic processes. We determined the periods of these pre-flare processes in an interval of 20 – 400 seconds by using special convolution filters and Fourier analysis. We propose to use this method to analyze active regions during the very early phases of solar flares, and even in real time.

Keywords Sun: solar flares · Moments · Frequency analysis · Pattern recognition

1. Introduction

There are various processing methods for analyzing solar active regions. The processing algorithms are designed for data observed by ground-based or satellite instruments considering the wavelength, time sequence, sampling frequency, temporal and spatial resolution,

S. Šimberová (✉) · M. Karlický
Astronomical Institute, Academy of Sciences of the Czech Republic, Ondřejov 251 65, Czech Republic
e-mail: ssimbero@asu.cas.cz

M. Karlický
e-mail: karlicky@asu.cas.cz

T. Suk
Institute of Information Theory and Automation, Academy of Sciences of the Czech Republic, Prague 8, 182 08, Czech Republic
e-mail: suk@utia.cas.cz

etc. Solar observations are made in a broad spectral range: from the shortest wavelengths of hard X-rays, followed by soft X-rays, extreme ultra-violet (EUV), via the optical lines up to the radio emission range. A detailed overview of image-processing techniques in solar physics, starting from the simple preprocessing algorithms up to 3D reconstructions, expert systems, and machine learning, has been given by Aschwanden (2010).

In addition to these image-processing methods, there are methods analyzing physical parameters measured in solar active regions. For example, Leka and Barnes (2003a, 2003b) used the statistical moments (mean, variance, skewness, and kurtosis) of magnetic-field parameters in active regions in searching for preflare signatures of solar flares.

The most common ground-based observations of solar active regions and solar flares are made in the Hα line. There is a global network of Hα observations monitoring solar activity for space-weather prediction: see, *e.g.*, www.ngdc.noaa.gov or bass2000.obspm.fr/home. For this purpose, an automatic processing system for solar-flare detection in Hα full-disk images has also been developed in the Kanzelhöhe Observatory (Veronig *et al.*, 2000). This system is based on the image-segmentation (region and edge detections) method.

While during a preflare phase the brightness at different locations of the active region on the Hα images continually varies, at the beginning of the flare the Hα brightness at flare ribbons strongly increases. This is due to particle beams and conduction fronts coming from the primary energy-release site in the low corona to the chromosphere, where the Hα line is formed, (*e.g.* Fárník *et al.*, 1983).

Each digital Hα image consists of pixels of different brightness. The brightness can be statistically described by its distribution as well as by the high-order statistical moments. These moments have applications in signal- and image processing (*e.g.* Albendea *et al.*, 2010; Jindal, Jindal, and Kaur, 2010) and in hyperspectral analysis (Chiang, Chang, and Ginsberg, 2001). In astrophysics they are used for example in investigating statistical system behavior, mass-density field distribution, statistical studies of the interstellar medium (Coles and Jones, 1991; Burkhart *et al.*, 2009), in pattern analysis of cosmic structure formation (Takada and Jain, 2002), statistical modeling of lines in atomic spectra (Pain *et al.*, 2009), detection of non-Gaussianity deviations (Grossi *et al.*, 2008), *etc.* A detailed study of the statistical moments in pattern recognition is given by Flusser, Suk, and Zitová (2009). The generalized spectral-kurtosis estimator (Nita and Gary, 2010b) and its statistics (Nita and Gary, 2010a) have been developed for a new generation of radio telescopes to detect and remove radio-frequency interference from radio-astronomy data. Another type of statistical moments considered in astronomical image-processing was described by Alipour, Safari, and Innes (2012), who used the Zernike moments for automatically detecting solar events observed in the EUV emission.

In this article we study the temporal evolution of the statistical moments (skewness and kurtosis) of Hα images of active regions during solar flares. We compare the moments computed for flaring and flare-quiet regions and search for preflare signatures.

Our article is organized as follows: The first two sections cover the theoretical background of the statistical moments, skewness and kurtosis filtering, and analysis methods. In Section 4 we describe the data specification, analysis, and results. Finally, the results are discussed.

2. The Statistical Moments – Skewness and Kurtosis

Simple statistical moments such as the mean $[EX]$, the standard deviation $[S = \sqrt{E(X - EX)^2}]$, and the high-order moments are used in pattern recognition as regional de-

scriptors. These functions quantitatively describe the structural shape of a region, its boundaries, texture content, *etc.* The use of moments in statistics is presented *e.g.* by Dudewicz and Mishra (1988).

The third moment about the mean $[\mu_3 = E(X - EX)^3]$ after scaling normalization is called the skewness $[m_3]$ of the distribution of the random variable $[X]$:

$$m_3 = \frac{1}{S^3} E(X - EX)^3. \tag{1}$$

The skewness is a measure of reflection symmetry, *i.e.* if the distribution of X is symmetric, then $\mu_3 = 0$. If the distribution is steeper to the left (right) of μ, it is denoted skewed to the right (left), respectively.

The fourth moment $[m_4]$ about the mean $[\mu_4 = E(X - EX)^4]$, called kurtosis, is defined similarly:

$$m_4 = \frac{1}{S^4} E(X - EX)^4. \tag{2}$$

It is used as a measure of how "heavy" the tails of distribution are, and expresses the peakedness. The distribution is said to be leptokurtic, platykurtic, or mesokurtic. The Gaussian distribution has $m_4 = 3$, therefore sometimes the value $\hat{m}_4 = m_4 - 3$ is used. When the platykurtic distribution with $\hat{m}_4 < 0$ is broader than Gaussian, the mesokurtic distribution has $\hat{m}_4 = 0$, *i.e.* the same kurtosis as Gaussian, and the leptokurtic distribution with $\hat{m}_4 > 0$ is narrower than Gaussian.

In discrete form we work with the realizations of X, and statistical characteristics as moments are only estimated, *e.g.* the average $[\mu]$ is an estimate of the mean $[EX]$ and the standard deviation $[\sigma]$ is an estimate of S. The dimensionless third and fourth moments are computed from the image histogram. In this sense the skewness of one image is estimated as the third moment normalized to scaling by the standard deviation

$$s = \frac{1}{\sigma^3} \frac{1}{N} \sum_{i=0}^{N-1} (x_i - \mu)^3, \tag{3}$$

and similarly the normalized fourth moment: kurtosis

$$k = \frac{1}{\sigma^4} \frac{1}{N} \sum_{i=0}^{N-1} (x_i - \mu)^4, \tag{4}$$

where x_i is the ith realization of the random variable $[X]$. In our case x_i is the brightness of the ith pixel of a chosen part in the Hα image, where N is the total number of pixels in the area.

In practice, we have an observational sequence of the Hα active-region images covering the time of solar flares. We compute the high-order moments $[s_i, k_i]$ of each image in the whole data sequence to obtain the temporal evolution of these moments. They express a flare-evolution in a new way, see *e.g.* Figure 1. It is very interesting to see the fast increase of both moments even before the GOES X-rays are increasing; time delays in cross-correlations between the skewness and GOES X-rays are given in Table 1. It indicates that the distribution of the pixel brightness changes rapidly at this time.

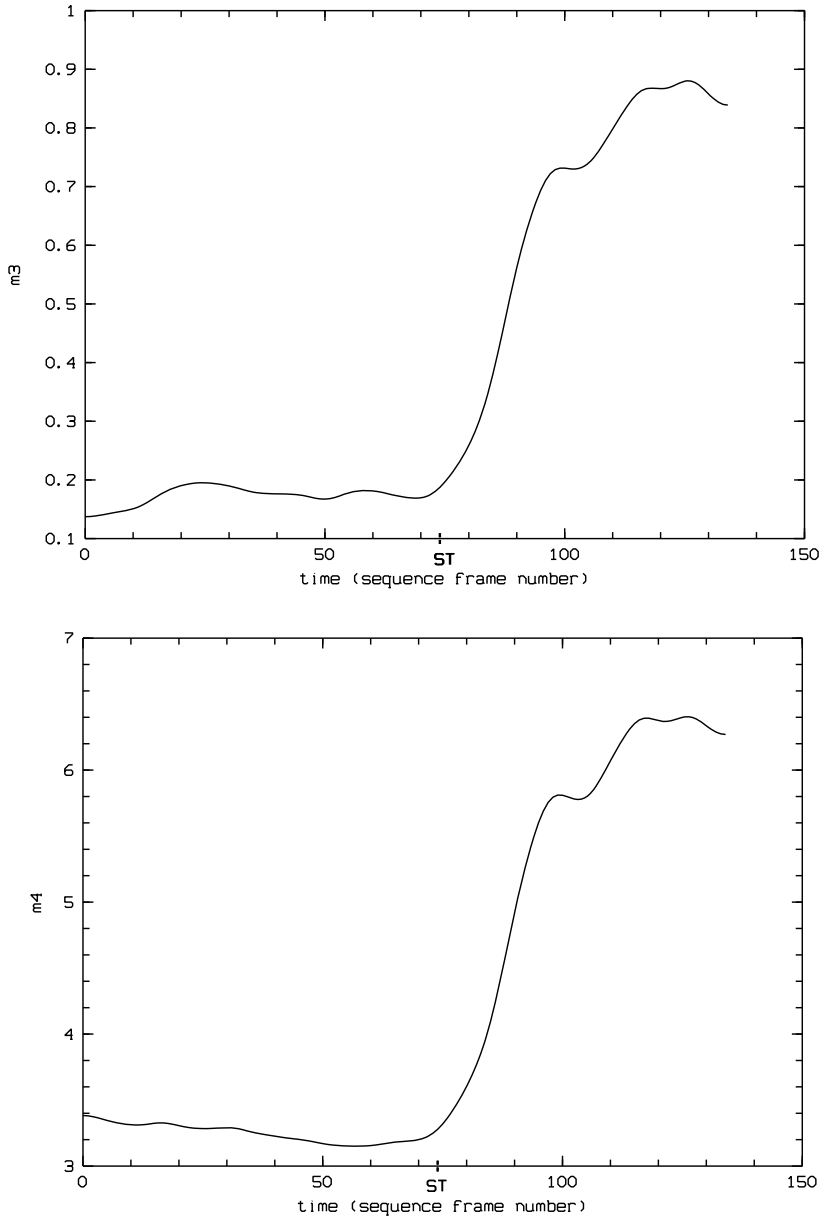

Figure 1 Typical temporal evolution of skewness (top) and kurtosis (bottom) during flare development. The moment's curve can be divided into two parts: preflare time interval, *i.e.* the time interval before the flare starting time (determined by an analysis of the moment evolution), and the time interval after this start time.

The observation is often distorted by high-frequency noise, therefore some type of filtering is appropriate. A simple filtering can be computed as the convolution

Table 1 Data specification – time intervals of the observed (processed) image data [UT], cadence in min^{-1}, the max. cross-correlation coefficient $\mathrm{CC}_{\max}$] between the skewness and GOES X-rays, the Kendall rank correlation coefficient KCRC, and corresponding GOES time delay against the skewness [s].

Label	Processed sequences		Cadence	$\mathrm{CC}_{\max}$	KCRC	Time delay
	Start	End				
O_030212	13:52	13:59	60	0.95	0.70	93
O_030221	14:58	15:13	20	0.98	0.66	27
O_030319	09:32	10:00	12	0.86	0.75	144
O_031218	12:25	12:43	12	0.90	0.69	42
K_110307	12:05	12:25	10	0.82	0.42	5
K_110910	07:04	07:31	10	0.90	0.59	0

$$s'_i = \sum_{j=-n_g}^{n_g} s_{i-j}\, g_j, \tag{5}$$

where $2n_g + 1$ is the length of the filter $[g]$. In the discrete case, the filter is a finite sequence of real numbers. An appropriate filter for our purpose should not change the signal amplitude or move the data, *i.e.* it should be energy-preserving and zero-mean:

$$\sum_{i=-n_g}^{n_g} g_i = 1, \qquad \sum_{i=-n_g}^{n_g} i g_i = 0. \tag{6}$$

It should also continuously include derivatives (*i.e.* be smooth), because each discontinuity causes a deterioration in the removal of high frequencies. Therefore the Gaussian with all continuous derivatives is very popular. We used a sampled version in the discrete case:

$$g_i = \frac{1}{\sigma_g \sqrt{2\pi}} \mathrm{e}^{-\frac{i^2}{2\sigma_g^2}}, \quad i = -n_g, -n_g + 1, \ldots, n_g, \tag{7}$$

where σ_g is the standard deviation of the filter that controls how high frequencies are filtered out. The half-width $[n_g]$ of the filter must be sufficient; it should be at least $n_g = 3\sigma_g$. We mostly used $n_g = 4\sigma_g$ in our experiments.

After filtering these moment curves, we searched for significant points (times) in these curves. We determined the flare start time defined here as the time at which there is a maximum of the second derivative of the skewness (kurtosis) curve. For other significant points, see Appendix A.

An analogy of the derivatives equaling zero in the continuous function are differences in changing its sign in the discrete case. These difference can be computed as the convolution with the first derivative filter $\{-1, 1\}$, similarly, the second derivative as the convolution with the Laplacian $\{1, -2, 1\}$. The third derivative can be estimated by the filter $\{-1, 3, -3, 1\}$, but we preferred to search for significant points as maxima of the Laplacian. The Gaussian and Laplacian can be combined into one filter, proposed in 2D by Marr and Hildreth (1980). The 1D version is

$$gl_i = \left(\frac{i^2}{\sigma_g^2} - 1 \right) \frac{1}{\sigma_g^3 \sqrt{2\pi}} \mathrm{e}^{-\frac{i^2}{2\sigma_g^2}}, \quad i = -n_g, -n_g + 1, \ldots, n_g. \tag{8}$$

The convolution filter in Equation (5) expects equidistant sampling, *i.e.* the time between adjacent samples is constant during the whole sequence. This is often not the case of a solar-flare data-cube. The sampling is mostly dense during the flare-up to the maximum with a slow decline after this interval (Veronig *et al.*, 2000). We considered the sampling density in the filtering and either interpolated missing data (which is more accurate) or changed σ_g according to the sampling. The decision depended on the data patterns and the investigated time segment.

3. Moment-Oscillation Analysis

There are several integral transformations for a signal temporal analysis. The traditional one is Fourier transformation [FT], see its normalized form in Appendix B. The FT can be understood as a decomposition of the signal into a weighted sum (linear combination) of sinusoidal functions with various frequencies. The harmonic u is expressed relative to the length n of the signal, *i.e.* the specific u means u oscillations per n samples. If the sampling frequency is f_s, then the actual frequency $f = f_s u/n$. If some harmonic $[u_s]$ is dominant in the signal, then the amplitude spectrum $[|F(u)|]$ has a significant local maximum at $u = u_s$. Typically, the global maximum is at $F(0)$, but it does not express any oscillations, therefore we are interested in all local maxima of $|F(u)|$ with the exception of that at zero in the oscillation analysis.

If the normalizing coefficient $[1/n]$ is used in the direct FT, amplitudes of two signals of different lengths can be compared more easily. We used resemblance $[\mathrm{rsb} = 2|F(u)|/n]$ in our experiments, because a pure sinusoidal function then has value unity at its frequency, so rsb can be understood as the ratio (in percent) of the analyzed signal to the ideal sinusoidal signal.

If the signal $f(x)$ is real, *i.e.* its imaginary part is zero, then the spectrum is reflectively symmetric and an analysis of the harmonics $u > n/2$ is meaningless. Moreover, the high harmonics are often distorted by noise and sampling errors, therefore we analyzed only low harmonics for $u = 1, 2, \ldots, 16$.

The formula for the inverse FT in Equation (11) implies that the FT is suitable for signal analysis, where the dominant frequencies are present throughout the whole sequence. If the signal is divided into small segments so that only one frequency is dominant in each segment and the different frequencies are dominant in other segments, then some other type of transformation is suitable, *e.g.* the wavelet transformation. If the signal can be divided into larger segments, where a few frequencies are dominant (as in our case), then a FT computed in this specified segment seems to be a more appropriate solution.

4. Real-Data Analysis

4.1. Data Specification

Two kinds of Hα data sets with different temporal and spatial resolution from the Kanzelhöhe and Ondřejov observatories were used. See an overview of the real data sets in Table 2.

The Kanzelhöhe sets contain full-disk observations, while those from the Ondřejov observatory are always the details with higher resolution; examples of one image of real data-cubes from Kanzelhöhe and Ondřejov are shown in Figure 2. As complementary data, GOES-8, -10, and -12 were used for additional information about the event. An active-region

Table 2 Analyzed events (label date syntax – year, month, day): K_yymmdd – Kanzelhöhe observation, O_yymmdd – Ondřejov observation.

Label	Event NOAA	Flare location	Flare			GOES X-ray classification
			Begin	Max	End	
O_030212	SF 7120	N11W26	13:54	14:00	14:15	B7.7
O_030221	SF 8310	N15E07	15:12	15:15	15:22	C3.7
O_030319	SF 3530	S15W57	09:42	09:52	09:57	M3.7
O_031218	SF 4480	N10E47	12:34	12:36	12:40	C2.9
K_110307	SF 1750	N10E19	12:20	12:21	12:23	C2.0
K_110910	SF 9350	N12W61	07:23	07:30	08:03	M1.1

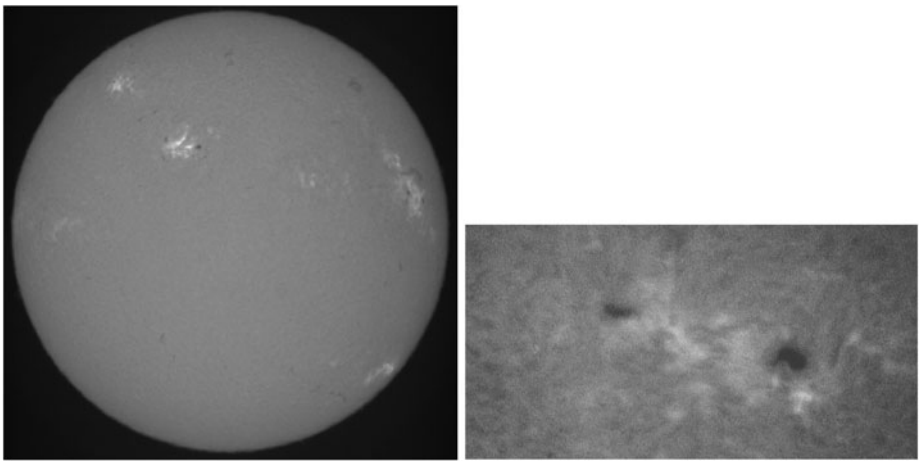

Figure 2 The full-disk observation – Kanzelhöhe (left), resolution 1 pix = 1.02 × 1.02 arcsec, the highest cadence is ten images per minute. The detail observation – Ondřejov (right), resolution 1 pix = 0.5 × 0.5 arcsec, customary cadence 60, 30, or 12 images per minute. Spatial extent: 347″ × 195″.

selection from the Kanzelhöhe sequence is shown in Figure 3. A plane of the image data-cube prepared for the Ondřejov sequence processing is shown in Figure 4. The different length of the processed sequences depends on the observational mode at each observatory.

4.2. Data Analysis

The mutual comparison of the m_3, m_4, and μ temporal evolution of the flare event observed at Ondřejov is presented in Figure 5. The moment's curves $m = f(t)$ of the skewness and kurtosis are very similar, and both unambiguously enable us to identify the flare starting time according to the above-mentioned methodology, see Figure 1. From the composed image in Figure 5 it is clearly visible that the low-order moments represented here by mean $[\mu]$ do not provide any relevant information about the position of the main zero of the third derivative, or "turning point"; see Appendix A for details. This time is important not only for determining the flare start but, for the oscillation analysis in the pre-flare times.

Additionally, we analyzed the behavior of the third and fourth moments simultaneously in a dynamically developing event and also in a quite region. Selecting two various areas

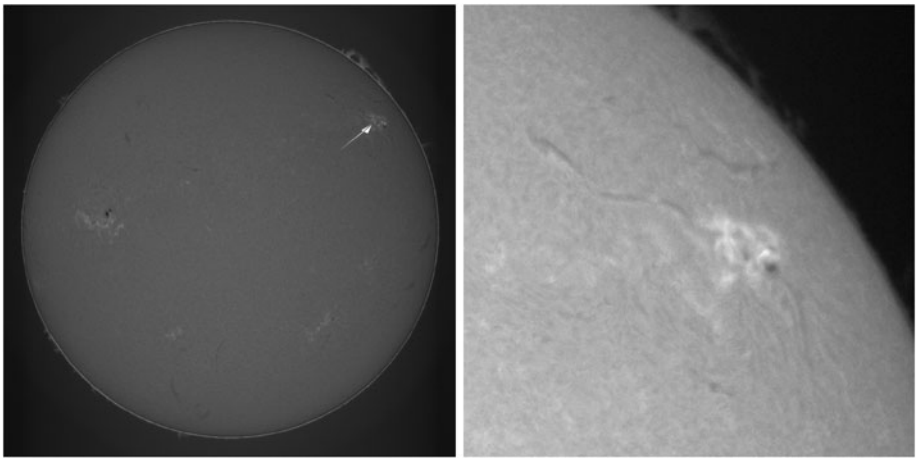

Figure 3 10 September 2011, Kanzelhöhe (left) full-disk observation 2048 × 2048 pix, (right) one plane of the subimage data-cube to be processed; resolution 1 pix = 1.02 × 1.02 arcsec. Spatial extent: $517'' \times 517''$.

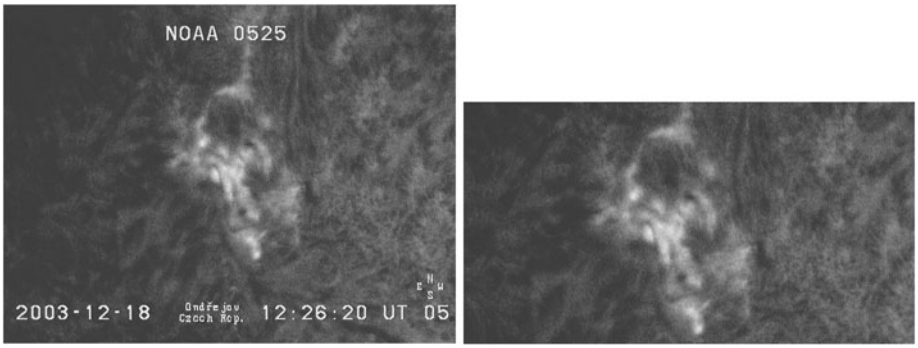

Figure 4 Ondřejov observation, (left) the original size 720 × 540 pix and (right) one sample of the data sequence prepared for processing. Resolution 1 pix = 0.5 × 0.5 arcsec. Spatial extent: $347'' \times 195''$.

enables the full-disk observation from Kanzelhöhe. The active and quiet regions are marked and their corresponding third moments are presented in Figure 6. The moments were computed in the same time-sequences; in the quiet region the values of m_3 vary around zero while m_3 of the active region with arising flare fluctuates with values more than one order higher.

An automatic significant-point search is shown in Figure 7. At first glance the course of $m_3 = f(t)$ already gives some information about important turning ponts during observation. Applying the Marr filter (Equation (8)) enables an automatic identification of changes in the noisy moment curve. The absolute maximum of the Marr-filter curve then determines the precise position of the main turning point assigned as the flare starting time. Likewise, the subsidiary maxima also give useful information, especially the period of maxima. The choice of the Marr-filter mask size depends on the type of data. The high-resolution data (Ondřejov) tend to need a smaller mask size (59 or 81 samples), while the data with lower resolution are analyzed by a mask of size 81 or 121 samples. According to our experiments, the mask size of 81 smaples is convenient and indicative for both types.

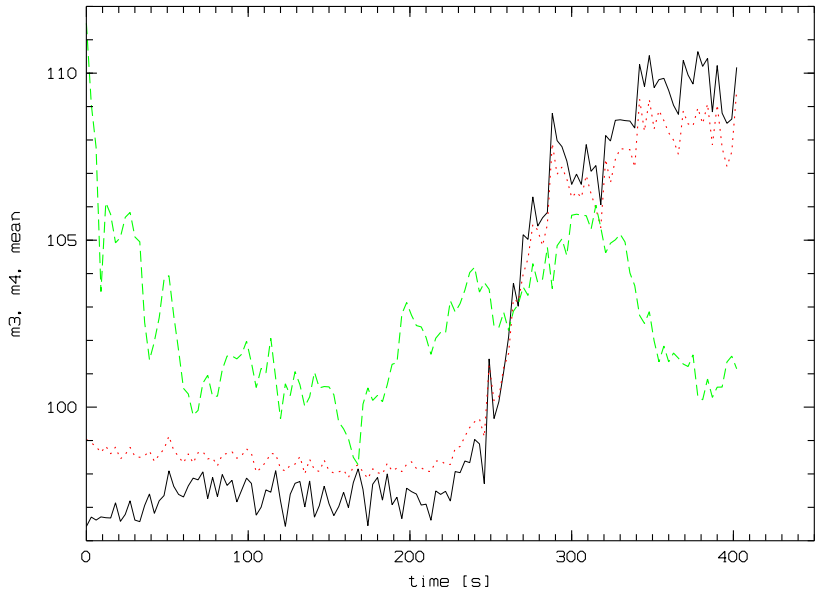

Figure 5 The skewness m_3 (black), kurtosis m_4 (dotted red), and mean μ (dashed green) of the Ondřejov observation O_030221 composed image. The zero-time in the plots is 14:58:16 UT.

We compared the moment curves with soft X-ray curves observed by the GOES satellites for all investigated events. The two examples of the Ondřejov and Kanzelhöhe events are shown in Figures 8 and 9. As can be seen here, the skewness curve roughly corresponds to the GOES one. Furthermore, the moments are much more sensitive to preflare activities than the GOES X-rays, showing strong variations of the moment at these times, in contrast to the smooth GOES curve. We also computed the cross-correlation coefficients and time delays between the skewness $[m_3]$ and GOES X-rays for all six events, see Table 1. We found very good correlations. Furthermore, in all events we found that the GOES X-ray curves are delayed (0 – 144 seconds). To obtain some information about the rank correlation, *i.e.* the similarity of the orderings of the data when ranked by each of the quantities, we computed the Kendall rank correlation coefficient

$$\tau = \frac{ccp - dcp}{\frac{1}{2}n(n-1)}, \tag{9}$$

where ccp is the number of concordant pairs, dcp is the number of discordant pairs, and n is the number of samples in the observed sequence. For details see Nelsen (2001). The coefficient must be in the range $-1 \leq \tau \leq 1$; if the agreement between the two rankings is perfect, the coefficient is 1. For reversible ranking $\tau = -1$, if both random-value sequences are independent, the coefficient is approximately zero. The values of coefficient τ (KCRC column) are listed in Table 1.

During solar flares, the light areas grow relative to the dark ones in Hα images. Therefore the right tail of the light-distribution function (*i.e.* histogram) is more significant than the light distribution of a quiet area. Both skewness and kurtosis are increasing during the rise of the flare. While these trends are common to all observations, the specific range of values varies with the observation mode (CCD camera specification and settings, sensing

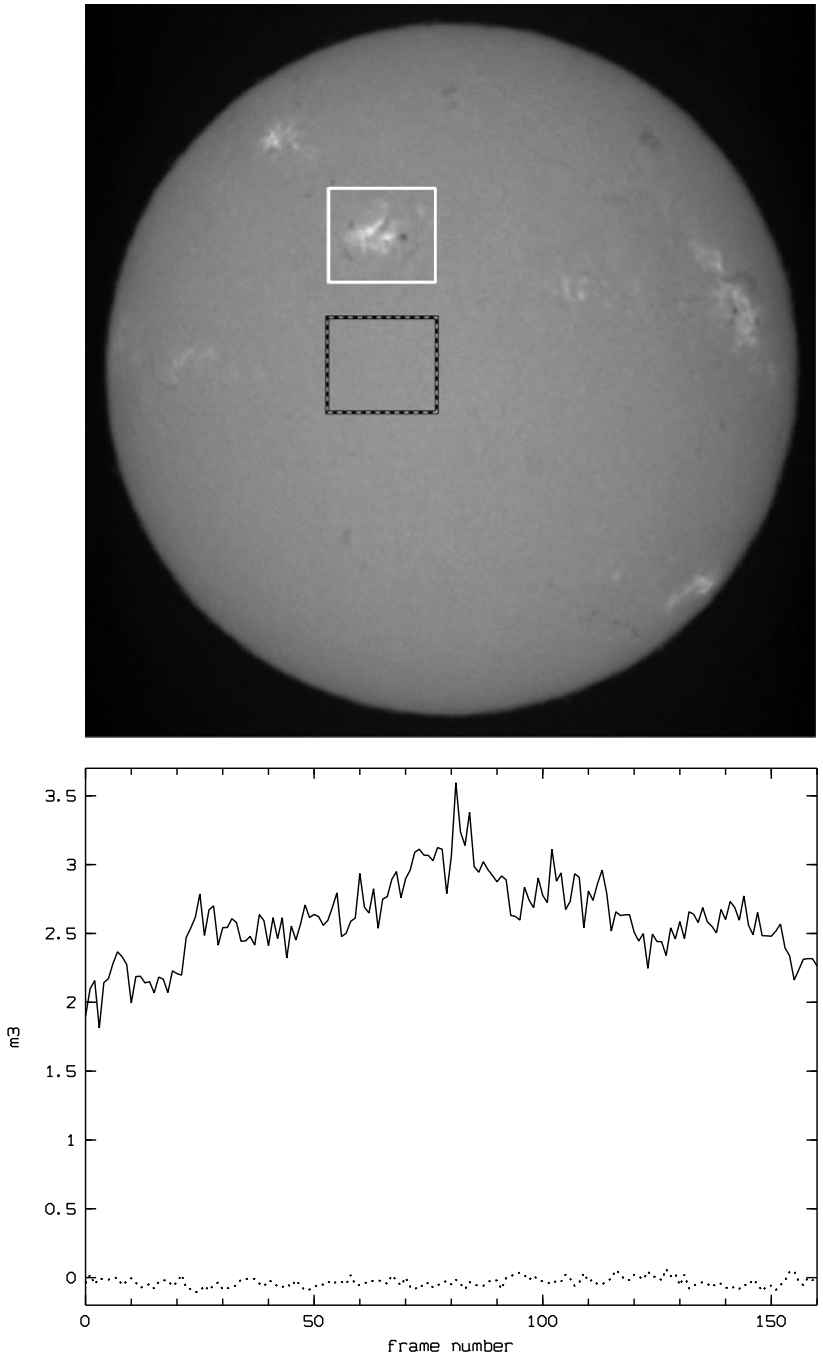

Figure 6 The full-disk Kanzelhöhe observation K_110307, subimages with an active and quiet area (top), the third moments – skewness of the corresponding sequences (bottom). The upper curve (solid) represents the third moments of the active region and the lower curve (dotted) the third moments of the quiet area, both with the same time-axes. The zero-time in the plot corresponds 11:30:39 UT.

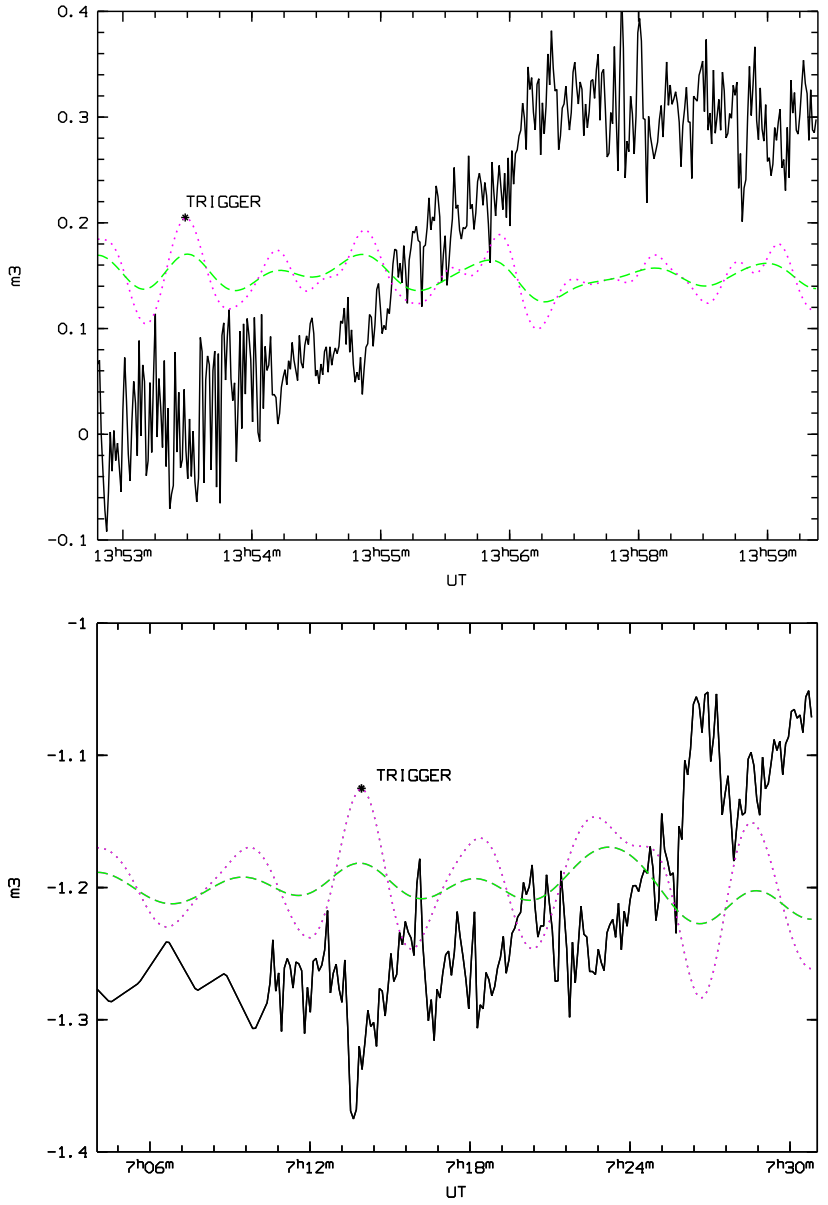

Figure 7 Significant and start points searching in the moment curves (black) and Marr-filter convolution (mask size 81 – dotted magenta line, mask size 121 – dashed green line). Upper panel – Ondřejov O_030212; lower panel – Kanzelhöhe K_110910.

threshold, contrast settings, *etc.*). For instance, in event O_030221, the original approximate Gaussian histogram with the skewness $m_3 \approx 0$ and kurtosis $m_4 \approx 3$ is deformed up to $m_3 \approx 1$ and $m_4 \approx 7$; see Figure 1. In the other events, m_3 varies from -1.3 (negative values – the distribution function is skewed to the left) to 3.7 (positive values – skewed to the right), and m_4 varies from 1.5 to 27 in our experiments.

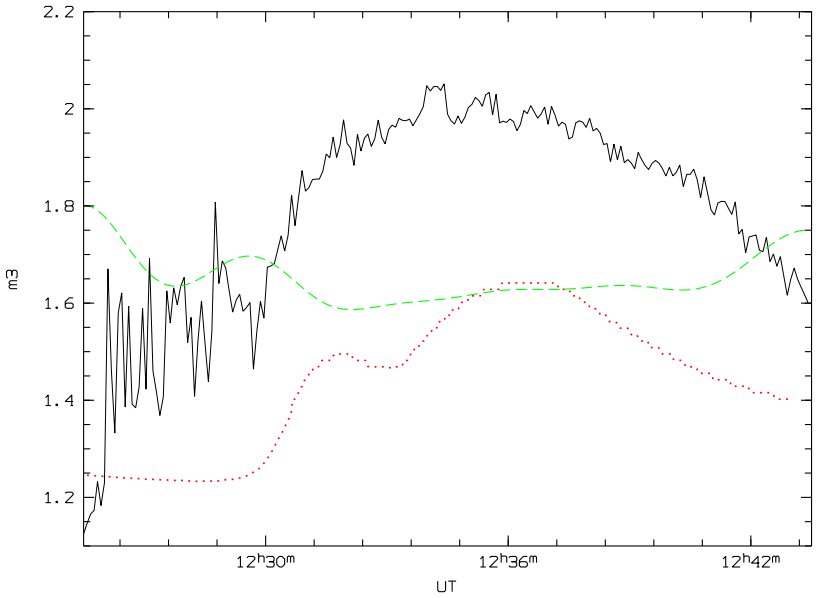

Figure 8 Skewness [m_3] over a period of the flare (black), its convolution with the Marr filter 121 (dashed green), and GOES-12 X-ray, 1.0 – 8.0 Å, three seconds (dotted red) for comparison in time. Observation Ondřejov O_031218.

Table 3 lists results of the time-sequence analysis of the studied events. The oscillation analysis was performed in the preflare times, close to the assigned start time. Events containing data more than 18 minutes before the flare starting-time show oscillations for the first frequency maxima at about four minutes and the second maxima at about two – three minutes.

Figure 10 shows the results of the oscillation analysis in two events. It shows the beginning of the amplitude spectrum from the first to the sixteenth harmonics with the most interesting frequencies. They were located using the local maxima converted to the oscillation periods in seconds (see Table 3).

5. Discussion and Conclusions

We presented a new method for flare diagnostics in a sequence of Hα active-region images. This method is based on computations of the high-order statistical moments of these images. Our experimental verifications on real-data sequences led to a determination of the flare starting time.

We found that time profiles of the Hα statistical moments during flares roughly correspond to those observed in soft X-rays by the GOES satellite. Furthermore, it was found that the maxima of the cross-correlation coefficients between the skewness and the GOES X-rays are 0.82 – 0.98, and the GOES X-rays are delayed 0 – 144 seconds relative to the skewness. The Kendall rank correlation coefficient provides interesting information concerning the association between the measured quantities m_3 and GOES.

We discovered an increased sensitivity of these moments to preflare activity; therefore we used the m_3 and m_4 moments to determine characteristic oscillations in the preflare phases. Periods of these oscillations were found in the interval of 20 – 400 seconds. These periods

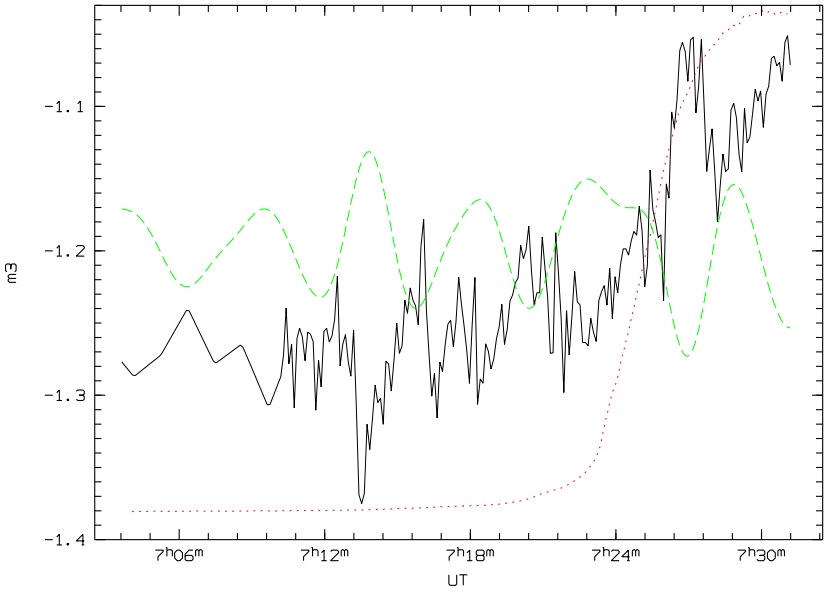

Figure 9 Skewness [m_3] over a period of the flare (black), its convolution with the Marr filter 81 (dashed green), and GOES-12 X-ray, 1.0 – 8.0 Å, two seconds (dotted red) for comparison in time. Observation Kanzelhöhe K_110910.

Table 3 Time-sequence analysis: The start means the beginning of the observed sequence, End_C is the end of sequence, End_A is the end of the analyzed preflare stage, ST is the flare starting-time. Format of time [hh:mm:ss]. Frequency analysis: max – positions of first and second maxima on harmonic scale, rsb – their resemblance to $\sin(x)$, $1/f$ – oscillation periods.

Event	O_031218	O_030319	O_030221	O_030212	K_110910	K_110307
Processed sequences						
Start	12:25:30	09:32:05	15:04:53	13:52:34	07:04:00	11:50:35
End_C	12:43:00	10:00:00	15:13:00	13:59:16	07:31:02	12:29:57
End_A	12:30:30	09:49:30	15:13:00	13:55:34	07:19:34	12:12:02
ST	12:29:00	09:48:15	15:08:51	13:53:24	07:13:16	12:08:05
Frequency analysis						
1.max	3.97	4.04	3.88	4.06	4.03	3.37
1.rsb[%]	10.74	4.52	1.75	2.97	2.41	8.58
$1/f_1$[s]	75.52	259.69	77.35	44.39	244.26	400.14
2.max	5.91	8.13	5.92	8.86	6.03	7.92
2.rsb[%]	6.82	2.94	1.00	1.32	1.11	3.74
$1/f_2$[s]	50.75	129.22	50.69	20.32	163.28	170.41

agree with those found in the preflare phases by Fárník, Karlický, and Švestka (2003) and Sych *et al.* (2009).

The advantage of our method is its uncommon robustness. It is possible to apply the method directly to the raw data sets; no preprocessing is required. It is much more robust

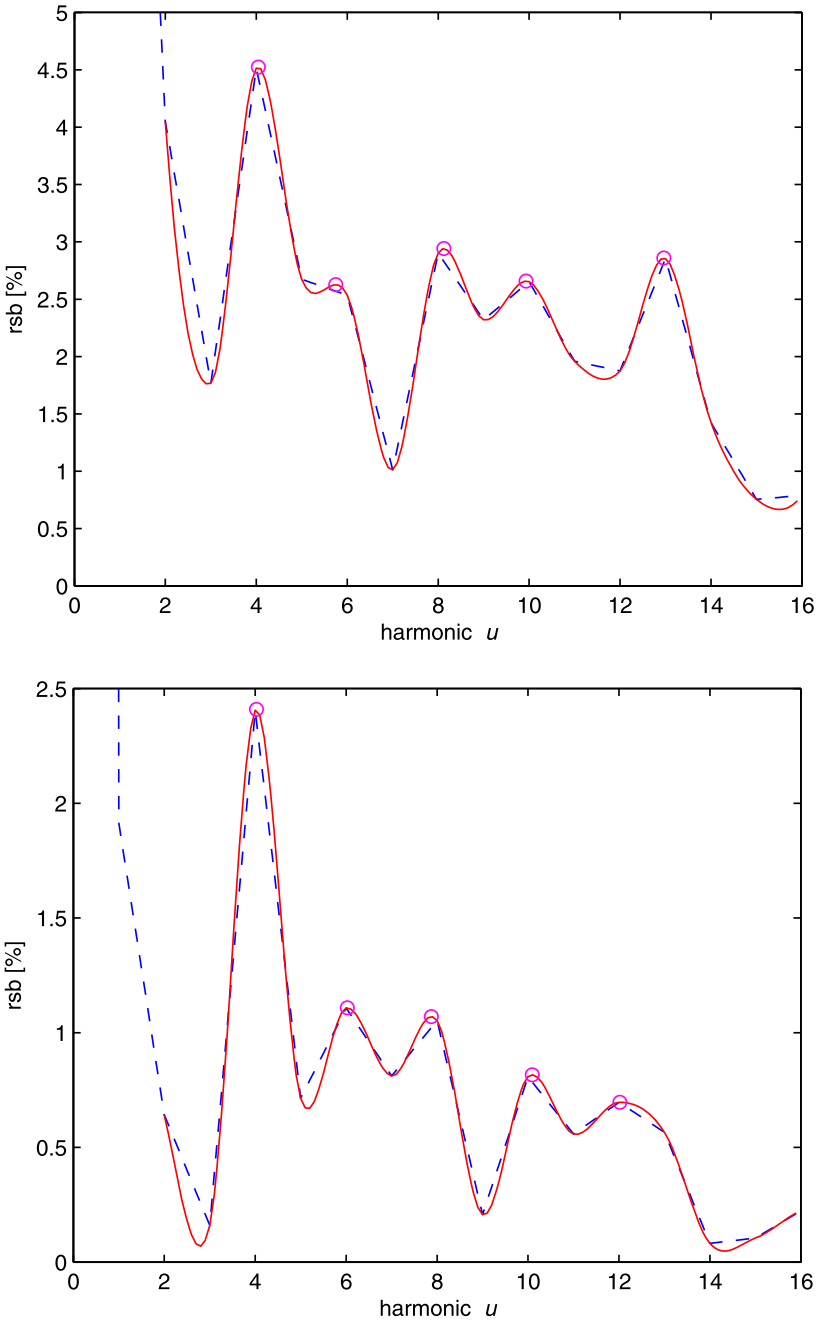

Figure 10 The result of the frequency analysis: Fourier amplitude spectrum (dashed blue) and its cubic spline with local maxima (solid red). Ondřejov observation O_030319 (top) and Kanzelhöhe observation K_110910 (bottom).

than methods using the light curve, for instance, and even more robust than the brightness average of the observed area.

For a comparison we applied the method to the data sequence of a quiet area without any apparent structural changes. The moments in time in these locations do not change noticeably; the absolute values of m_3 varied around 0 and those of m_4 around 3, with standard deviation in both cases of about 0.02.

For an automatic turning point search in the moment function $m_3 = f(t)$ we suggested filtering by a special convolution filter that combines the Gaussian for noise reduction and the second derivative. The local maxima of the second derivative indicate certain breaks in the observed time-sequence. Likewise, the period of these local maxima is interesting. A more detailed study of this variable could be a topic of future work.

We found that the moments are very sensitive to changes in the image brightness in the preflare phase. For this reason we propose to use this method not only for the analysis of the preflare phases of previously observed solar flares, but also for the analysis of these phases in real time. This method can be used to analyze flare observations in other spectral bands as well.

Acknowledgements In memory of Zdeněk Švestka and the twentieth anniversary of our joint paper in *Solar Physics* **146**, 1993. Stana Šimberová and Marian Karlický, March 2013.

The authors thank the anonymous referee for comments that improved the article. This research was supported by the Czech Science Foundation GAČR 102/08/1593, GAČR P209/12/0103 and GAČR P103/11/1552. Thanks to Astrid Veronig and Wolfgang Hirtenfellner-Polanec (Universität Graz and Observatory Kanzelhöhe), and František Zloch (Observatory Ondřejov) for their help with accessing image databases and event hunting.

Appendix A: Significant Curve Points

The significant points on a smooth curve can be searched for by using its derivatives. The zero-crossings are assumed to be found directly either as a solution of an equation, or numerically. An extremum (minimum or maximum) can be found as the zero-crossing of its first derivative. Similarly, we can use the second derivative to search for inflection points. If there is a zero-crossing of the third derivative, we can describe it as a turning point, or change of trend, where an increase changes to a steeper (gentler) increase, or a decrease to a steeper (gentler) decrease. An overview of the significant points is provided in Table 4. If the derivative in the first column equals zero, the curve in the first row has the significant point.

Table 4 Identification of functional significant points.

	$f(x)$	$f'(x)$	$f''(x)$	$f'''(x)$
$f(x) = 0$	Zero-crossing			
$f'(x) = 0$	Extreme	Zero-crossing		
$f''(x) = 0$	Inflection point	Extreme	Zero-crossing	
$f'''(x) = 0$	Turning point	Inflection point	Extreme	Zero-crossing

Appendix B: Discrete Fourier Transformation

The Fourier transformation [FT] is defined in the discrete case

$$F(u) = \sum_{k=0}^{n-1} f(x_k) \mathrm{e}^{-2\pi \mathrm{i} u k/n}, \quad u = 0, 1, \ldots, n-1. \tag{10}$$

k is the ordinal number of the sample, u is the harmonic, $u = 1$ is the fundamental harmonic, $u = 2, 3, \ldots$ are second, third, *etc.* harmonics.

The signal can be recovered by inverse FT

$$f(x_k) = \frac{1}{n} \sum_{u=0}^{n-1} F(u) \mathrm{e}^{2\pi \mathrm{i} u k/n}, \quad k = 0, 1, \ldots, n-1. \tag{11}$$

The normalizing factor $\frac{1}{n}$ can be either in the direct transformation (Equation (10)), in the inverse one (Equation (11)), or $\frac{1}{\sqrt{n}}$ can be in both. In the first case, $F(0)$ is the sum of all values of the signal, in the second case, $F(0)$ becomes the mean value of the signal. Typically, this is the global maximum of the amplitude spectrum.

References

Albendea, P., Madruga, F.J., Cobo, A., López-Higuera, J.M.: 2010, Signal to noise ratio (SNR) comparison for pulsed thermographic data processing methods applied to welding defect detection. In: Maldague, X.P.V. (ed.) *10th International Conference on Quantitative InfraRed Thermography QIRT'10, IEEE – Section de Québec*, É. du Cao, 8.

Alipour, N., Safari, H., Innes, D.E.: 2012, An automatic detection method for extreme-ultraviolet dimmings associated with small-scale eruption. *Astrophys. J.* **746**, 12. doi:10.1088/0004-637X/746/1/12.

Aschwanden, M.J.: 2010, Image processing techniques and feature recognition in solar physics. *Solar Phys.* **262**(2), 235 – 275. doi:10.1007/s11207-009-9474-y.

Burkhart, B., Falceta-Gonçalves, D., Kowal, G., Lazarian, A.: 2009, Density studies of MHD interstellar turbulence: statistical moments, correlations and bispectrum. *Astrophys. J.* **693**, 250 – 266. doi:10.1088/0004-637X/693/1/250.

Chiang, S.-S., Chang, C.-I., Ginsberg, I.W.: 2001, Unsupervised target detection in hyperspectral images using projection pursuit. *IEEE Trans. Geosci. Remote Sens.* **39**(7), 1380 – 1391.

Coles, P., Jones, B.: 1991, A lognormal model for the cosmological mass distribution. *Mon. Not. Roy. Astron. Soc.* **248**, 1 – 13.

Dudewicz, E.J., Mishra, S.N.: 1988, *Modern Mathematical Statistics*, Wiley, New York.

Fárník, F., Karlický, M., Švestka, Z.: 2003, Hard X-ray pulsations in the initial phase of flares. *Solar Phys.* **218**, 183 – 195. doi:10.1023/B:SOLA.0000013044.61171.d9.

Fárník, F., Valnicek, B., Kalman, B., Kaastra, J., Slottje, C., Karlický, M.: 1983, X-ray, H-alpha, and radio observations of the two-ribbon flare of 16 May, 1981. *Solar Phys.* **89**, 355 – 378. doi:10.1007/BF00217256.

Flusser, J., Suk, T., Zitová, B.: 2009, *Moments and Moment Invariants in Pattern Recognition*, Wiley, New York.

Grossi, M., Branchini, E., Dolag, K., Matarrese, S., Moscardini, L.: 2008, The mass density field in simulated non-Gaussian scenarios. *Mon. Not. Roy. Astron. Soc.* **390**, 438 – 446. doi:10.1111/j.1365-2966.2008.13783.x.

Jindal, R., Jindal, S., Kaur, N.: 2010, Analyses of higher order metrics for SPIHT based image compression. *Int. J. Comput. Appl.* **1**(20), 56 – 59.

Leka, K.D., Barnes, G.: 2003a, Photospheric magnetic field properties of flaring versus flare-quiet active regions. I. Data, general approach, and sample results. *Astrophys. J.* **595**, 1277 – 1295. doi:10.1086/377511.

Leka, K.D., Barnes, G.: 2003b, Photospheric magnetic field properties of flaring versus flare-quiet active regions. II. Discriminant analysis. *Astrophys. J.* **595**, 1296 – 1306. doi:10.1086/377512.

Marr, D., Hildreth, E.: 1980, Theory of edge detection. *Proc. Roy. Soc. London B, Biol. Sci.* **207**(1167), 187 – 217.

Nelsen, R.B.: 2001, Kendall tau metric. In: Hazewinkel, M. (ed.) *Encyclopedia of Mathematics*, Springer, Berlin.

Nita, G.M., Gary, D.E.: 2010a, Statistics of the spectral kurtosis estimator. *Publ. Astron. Soc. Pac.* **122**, 595 – 607. doi:10.1086/652409.

Nita, G.M., Gary, D.E.: 2010b, The generalized spectral kurtosis estimator. *Mon. Not. Roy. Astron. Soc.* **406**, L60 – L64. doi:10.1111/j.1745-3933.2010.00882.x.

Pain, J.-C., Gilleron, F., Bauche, J., Bauche-Arnoult, C.: 2009, Effect of third- and fourth-order moments on the modeling of unresolved transition arrays. *High Energy Density Phys.* **5**, 294 – 301. doi:10.1016/j.hedp.2009.05.001.

Sych, R., Nakariakov, V.M., Karlický, M., Anfinogentov, S.: 2009, Relationship between wave processes in sunspots and quasi-periodic pulsations in active region flares. *Astron. Astrophys.* **505**, 791 – 799. doi:10.1051/0004-6361/200912132.

Takada, M., Jain, B.: 2002, The kurtosis of the cosmic shear field. *Mon. Not. Roy. Astron. Soc.* **337**, 875 – 894. doi:10.1046/j.1365-8711.2002.05972.x.

Veronig, A., Steinegger, M., Otruba, W., Hanslmeier, A., Messerotti, M., Temmer, M., Brunner, G., Gonzi, S.: 2000, Automatic image segmentation and feature detection in solar full-disk images. In: Wilson, A. (ed.) *The Solar Cycle and Terrestrial Climate, Solar and Space Weather* **SP-463**, ESA, Noordwijk, 455.